Journal of
Synchrotron
Radiation

ISSN 1600-5775

Received 2 December 2013
Accepted 7 May 2014

Towards tender X-rays with Zernike phase-contrast imaging of biological samples at 50 nm resolution

Ismo Vartiainen,[a]* Martin Warmer,[b] Dennis Goeries,[b] Eva Herker,[c] Rudolph Reimer,[c] Christian David[a] and Alke Meents[b]

[a]Paul Scherrer Institut, Villigen PSI, Switzerland, [b]Deutsches Elektronen-Synchrotron (DESY), Hamburg, Germany, and [c]Heinrich-Pette-Institute, Leibniz Institute for Experimental Virology, Hamburg, Germany. *E-mail: ismo.vartiainen@psi.ch

X-ray microscopy is a commonly used method especially in material science application, where the large penetration depth of X-rays is necessary for three-dimensional structural studies of thick specimens with high-Z elements. In this paper it is shown that full-field X-ray microscopy at 6.2 keV can be utilized for imaging of biological specimens with high resolution. A full-field Zernike phase-contrast microscope based on diffractive optics is used to study lipid droplet formation in hepatoma cells. It is shown that the contrast of the images is comparable with that of electron microscopy, and even better contrast at tender X-ray energies between 2.5 keV and 4 keV is expected.

Keywords: X-ray microscopy; biological samples; Zernike phase contrast.

1. Introduction

During the last years, X-ray microscopy (XRM) has become a very powerful technique. Similar to light microscopy (LM) and electron microscopy (EM), XRM can be performed both in scanning and in full-field mode. In scanning transmission X-ray microscopy (STXM) the X-rays are focused into a very small spot size of a few tens of nanometers only and the sample is scanned. In contrast to scanning electron microscopy (SEM), X-rays are not charged and thus cannot be deflected in a magnetic field such as in EM. In most cases the sample has therefore to be mechanically scanned. Thus STXM requires very precise and stable mechanics on the single digit nanometer level especially with respect to long-term thermally induced drifts. Since this is experimentally very demanding, mechanical instabilities are often regarded as one of the main resolution-limiting factors in XRM (Dierolf *et al.*, 2010).

This need to mechanically move the sample with respect to the X-ray beam can be avoided in so-called full-field microscopy. Similar to classical LM, a large area of the sample is illuminated and an objective lens is used to generate a magnified image of the sample. Owing to the relatively weak interaction of X-rays with matter compared with electrons, X-ray microscopy has also the advantage of being able to penetrate through thicker samples and is therefore ideally suited for tomography.

A special case of X-ray microscopy is coherent diffractive imaging (CXDI), also referred to as lensless imaging, where the sample is coherently illuminated and no objective lens is placed between the sample and the detector. Here, the far-field diffraction pattern is recorded with the detector and the Fourier back-transform is iteratively computed by applying certain constraints to the sample. A combination of both CXDI and STXM, referred to as ptychography, turned out to be a very powerful method (Thibault *et al.*, 2008). In ptychography the sample is coherently illuminated with a relatively small beam. With this technique spatial resolutions of sub-10 nm have been recently achieved in experiments with highly scattering inorganic samples (Vila-Comamala *et al.*, 2011; Schropp *et al.*, 2012; Holler *et al.*, 2012). Even though STXM and ptychography can be applied to tomography, the required scanning times in these pointwise methods are long for each projection, and full tomographic data sets of dynamic specimens, and in cases where statistics are required, are in practice unattainable with these methods. Hence, X-ray full-field microscopy is a very powerful technique for three-dimensional imaging.

Compared with X-ray microscopy in environmental and material science where often high-Z elements are present, biological samples mainly consist of light elements such as carbon, oxygen and nitrogen (Henke *et al.*, 1993) providing only poor absorption contrast. In order to increase contrast, while maintaining the required penetration depth, contrast enhancement methods need to be applied. Zernike phase-contrast microscopy (Zernike, 1935; Born & Wolf, 1999) can be applied for samples that are too weakly absorbing and affect only the phase of the penetrating X-rays. This method, adopted from visible-light microscopy, transfers the phase shift induced by the sample to amplitude differences in the detector plane by adding a phase shifter to the back focal plane of the objective lens. This method has been successfully applied in full-field X-ray microscopy with various photon energies (Schmahl *et al.*, 1995; Neuhäusler *et al.*, 2003; Chu *et al.*, 2008; Stampanoni *et al.*, 2010).

doi:10.1107/S1600577514010388

X-ray microscopy in the water window has become a powerful tool during the last years and isotropic resolutions of down to 30 nm could be achieved in tomographic mode. However, sample thickness in high-resolution three-dimensional imaging in the water window with X-ray microscopy is very limited as the depth of focus (DOF) scales down with the photon energy (or with the inverse of the wavelength). Therefore, this energy range has limitations with biological imaging, where the thickness of the cells ranges from a few micrometers to a few tens of micrometers. Recent calculations revealed that the optimal energy for such experiments is around tender X-ray energies at 2.5 keV (Wang *et al.*, 2013).

Different imaging X-ray optics can be used for XRM. Whereas X-ray refractive optics, also referred to as X-ray lenses, are mainly used for hard X-rays with energies above 10 keV (Snigirev *et al.*, 1996), at lower energies diffractive optics such as Fresnel zone plates (FZPs) are preferably used since they cause less absorption losses (David *et al.*, 2000). In addition, FZPs provide high resolution down to 10 nm defined by the outermost zone width. Combined with a large acceptance aperture and simple alignment, they provide efficient means for nanofocusing at tender X-ray photon energies.

It was the goal of the present work to explore the resolution and contrast which can be achieved with Zernike X-ray full-field microscopy of biological samples.

2. Experimental

Hepatitis C virus (HCV) is a positive-strand RNA virus that replicates in the cytoplasm of liver cells. In recent studies, lipid droplets, the cellular storage organelles for neutral lipids, emerged as putative viral assembly sites (Herker & Ott, 2011). Interestingly, liver steatosis, which is an abnormal accumulation of lipid droplets in liver cells, is a frequent symptom of HCV infection that might negatively influence treatment responses. As a proof-of-principle experiment for the study of this HCV-associated lipid droplet formation, Huh7 hepatoma cells were treated with oleic acid which leads to the formation of lipid droplets similar to those arising from HCV infection, without the need to work with infectious material.

2.1. Sample preparation

The protocol for the sample preparation is based on methods established in electron microscopy to guarantee good preservation of the cellular structure. Further requirements were the stability of the sample in the X-ray beam and high contrast of the structures of interest. Huh7 cells were grown on 30 nm silicon nitride windows (SILSON Ltd). Cells were fixed with paraformaldehyde (4%) and glutaraldehyde (2.5%). Osmium tetroxide was used for post-staining and the cells were additionally contrasted with uranyl acetate. Dehydration was carried out in a graded ethanol series and finally the cells were air-dried from trichlorotrifluoroethane.

2.2. Measurement set-up

The design of the microscope is based on beam shaper illumination as a condenser (Vartiainen *et al.*, 2014; Vogt *et al.*, 2006). The beam shaper consists of trapezoids with constant period and fringe orientation arranged in a circular grid. The diameter of the condenser is 900 µm, its outermost zone width is 50 nm and the thickness of the zones is 700 nm. As an objective lens we used a 150 µm-diameter FZP with a numerical aperture matched to that of the condenser. Both of the components were fabricated by electron beam lithography and gold electroplating. This configuration ideally leads to a Rayleigh resolution of $1.22\Delta r$, where Δr is the outermost zone width of the condenser and FZP. For the Zernike phase contrast, a phase shifter is placed to the back focal plane of the objective lens.

Experiments were performed at beamline P11 at the PETRA III synchrotron at DESY in Hamburg. A detailed description of the beamline and optical system can be found elsewhere (Meents *et al.*, 2013). An X-ray energy of 6.2 keV was chosen for the experiments as a compromise between phase contrast of the sample and air absorption since an in-vacuum set-up is not available yet at P11. A schematic drawing of the experimental set-up is shown in Fig. 1.

The sample is uniformly illuminated by the beam shaper, and the scattered and unscattered light from the sample is collected by the objective lens. A phase shifter designed to phase shift only the unscattered light is placed to the back focal plane (BFP) of the objective lens. The phase shifter is made of silicon with structure height of 3.9 µm to produce a phase shift of $\pi/2$ at 6.2 keV photon energy. As these two light paths propagate to the detector plane, they interfere, thus revealing the phase shift produced by the sample. Two kinds of contrast modes can be applied in Zernike phase-contrast microscopy: so-called negative phase contrast is achieved by phase shifting the unscattered wave by $-\pi/2$ (or $3\pi/2$) compared with the scattered one, whereas a positive phase-contrast image is achieved by $\pi/2$ phase shift to the unscat-

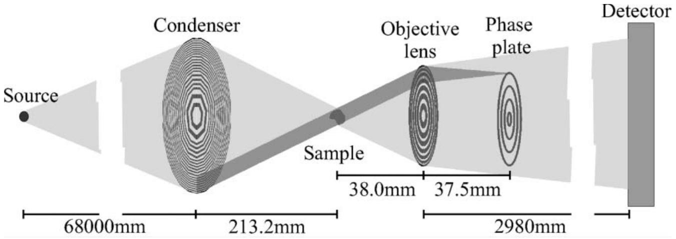

Figure 1
Schematic drawing of the X-ray Zernike phase-contrast set-up. The unfocused X-ray beam with a size of ~900 µm × 1200 µm at a distance of 68 m from the source passes a segmented condenser which focuses the beam to a circular spot of 50 µm diameter defined by the overlap of subfields in the condenser. The central part of the beam is blocked by a central stop with a diameter of 450 µm located a few millimeters before the condenser. An order-sorting aperture with an inner diameter of 250 µm is used to block the zeroth and higher-order contributions from the condenser. The light path of the first diffraction order from the beam shaper that is not scattered by the sample is depicted in dark gray. The central stop and the order-sorting aperture were omitted for clarity.

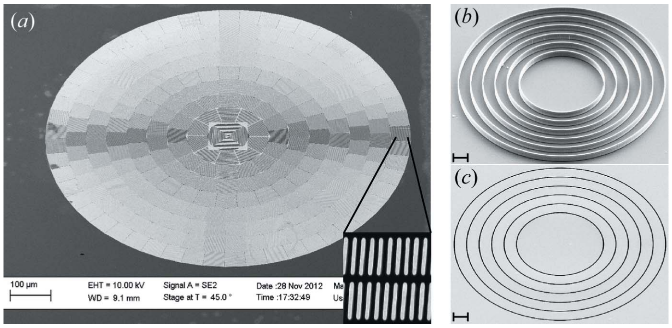

Figure 2
SEM images of the beam shaper condenser (*a*) and negative (*b*) and positive tone (*c*) phase shifters. The inset in (*a*) shows the 50 nm outermost zones of the beam shaper. The scale bars in (*b*) and (*c*) are 10 µm.

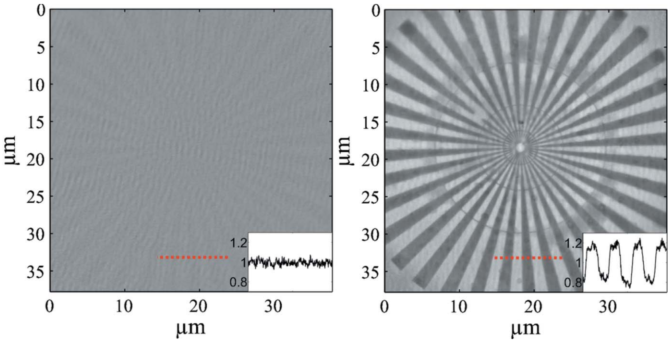

Figure 4
Ni Siemens star imaged with absorption (left) and negative phase-contrast mode (right). The scaling of the intensities is identical for good comparison. The insets present the cross sections along the dotted red lines.

tered wave compared with the scattered one. The distances shown in Fig. 1 lead to a magnification factor of 78. Fig. 2 shows SEM images of the beam shaper condenser and phase-shifting rings. It should be noted that the central rings are omitted from the phase plate since they are not illuminated due to the central stop in front of the condenser.

The resulting X-ray image was indirectly recorded by a 30 µm-thick cerium-doped YAG screen with a PCO edge camera equipped with a 4× magnifying Olympus microscope objective (NA = 0.5). The resolution of the camera system was determined to 1.7 µm. The theoretical detection efficiency of the system was calculated to be 0.12.

A series of test samples was imaged to evaluate the performance of the microscope, and to compare the contrast between absorption and Zernike phase-contrast modes. As test samples we used Siemens stars fabricated by electron beam lithography and nickel or gold electroplating. The thickness of the gold and nickel structures was 700 nm and 200 nm, leading to 40% and 1.5% absorption, respectively, at 6.2 keV. Fig. 3 shows a contrast comparison of the two modes with an Au Siemens star as a test sample. The scaling of the intensities is identical in both of the images, which clearly shows that phase contrast is very beneficial even for this relatively absorbing sample. Fig. 4 shows the contrast comparison in the case of weakly absorbing Ni structures with identical intensity scaling. Absorption contrast is very low in the case of Ni structures, as expected from the theoretical transmission value. However, in phase-contrast mode, all the structures are well visible.

Before investigating the biological sample, a positive phase shifter was placed at the BFP of the objective lens, and the alignment was verified by imaging a test structure. Fig. 5 (left) shows an experimental Zernike phase-contrast image of a nickel Siemens star used as a test sample. The thickness of the Ni was 400 nm leading to absorption of 3% and phase shift of $\pi/6$. The inset shows the 50 nm innermost spokes. Fig. 5 (right) shows a ZPC image of a hepatoma cell. Typical features of the cell are clearly visible.

For direct comparison, electron microscopy images were taken from the same samples after the X-ray imaging experiment. Fig. 6 shows a direct comparison of the same Huh7 cell imaged with X-ray and electron microscopy. The electron micrograph was taken with variable-pressure environmental scanning electron microscope mode (VP-ESEM) at 1 Torr pressure and 20 keV acceleration voltage by using a backscattered electron detector. On both images the same features can be observed. Importantly, lipid droplets are clearly visible in the X-ray image.

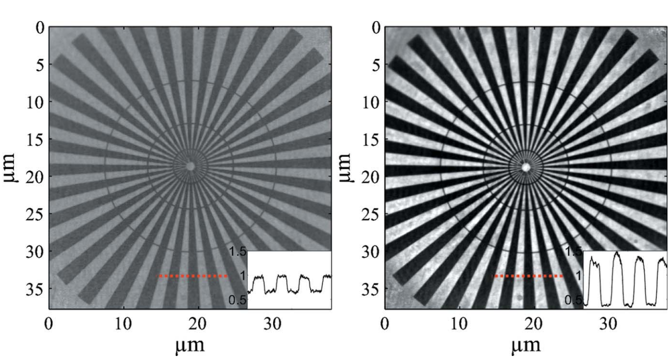

Figure 3
Au Siemens star imaged with absorption (left) and negative phase-contrast mode (right). The scaling of the intensities is identical for good comparison. The insets present the cross sections along the dotted red lines.

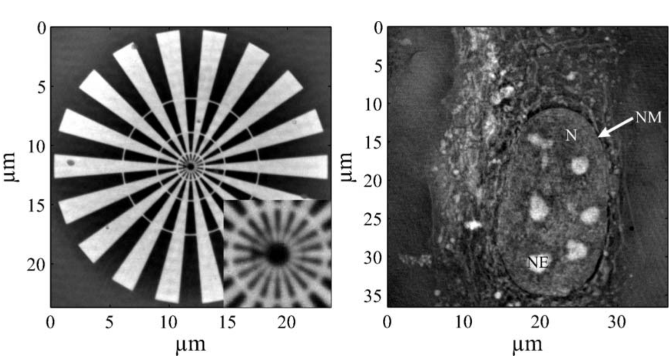

Figure 5
ZPC images of a test structure (left) and a monolayer liver cell (right). The inset in the left image shows the 50 nm innermost spokes of the test structure. The image of the cell clearly features the expected components of the cells, such as nucleus (N), nucleolus (NE) and nuclear membrane (NM).

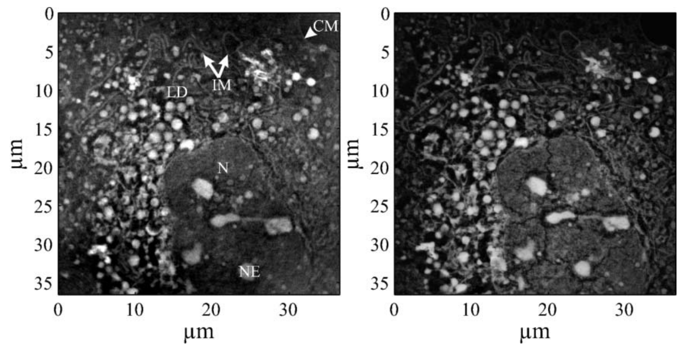

Figure 6
X-ray ZPC image (left) and a corresponding electron micrograph (right) of a hepatoma cell treated with oleic acid. Lipid droplets (LD) as well as common cell organelles: nucleus (N), nucleolus (NE), cellular membrane (CM) and internal membranes (IM) are clearly visible.

To estimate the resolution in the case of biological objects, we performed a radial power spectrum analysis on the images shown in Fig. 6. To calculate the averaged power spectrum we took a Fourier transform from the image and transferred it to polar coordinates. The amplitude was calculated by taking a mean value of the amplitude over the angles for different radii and scaled with the amplitude of the zero frequency. Saturation of the curve defines the limit after which there are no frequencies present in the original figures. Fig. 7 represents the power spectrum images of the X-ray microscopy image and the SEM image. As can be seen, the resolution in the X-ray image is around 50 nm, after which the amplitude of the power spectrum soon reaches saturation, whereas the resolution of the SEM image is limited by the pixel size of 35 nm.

3. Conclusions and outlook

Our first experiments show that X-ray Zernike phase-contrast microscopy is a very powerful method for imaging of biological samples providing only poor absorption contrast. The experiments clearly show that a resolution of 50 nm can be achieved with biological samples. Even smaller isolated features such as the nuclear membrane with a thickness of 14 nm only could be identified on the images. Experiments applying this method in 3D by computed tomography are already scheduled.

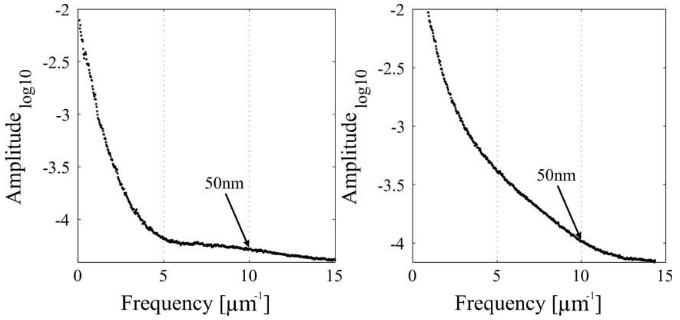

Figure 7
Radially averaged power spectra of the X-ray ZPC image (left) and the electron micrograph (right) computed from Fig. 6. 50 nm feature size is indicated in both images.

In the future, we plan to further increase the spatial resolution down to 20 nm which is then comparable with what can be currently achieved with biological samples in the water window. Tender X-rays, having typical X-ray energies between 2 keV and 5 keV, are located between the soft X-ray regime with energies below 2 keV, which strictly require in-vacuum operation, and the hard X-ray regime with energies above 5 keV, where experiments can be performed in air. Tender X-rays have not been commonly used in X-ray science over the last decades but have recently drawn attention for several applications, among other fields also for the investigation of biological samples due to the better scattering contrast than at higher X-ray energies. The new set-up is foreseen to operate at tender energies between 2.5 and 4 keV and we expect much better contrast compared with the present experiments at 6.2 keV due to a larger phase shift of the light elements in the biological specimens at lower photon energies. This will allow us to perform high-resolution experiments even with unstained samples. This experiment will be operated in-vacuum and allow for cryogenic sample cooling in order to reduce radiation damage effects (Meents *et al.*, 2013). Owing to the larger depth of field we expect to achieve a better isotropic resolution than what can be currently achieved by soft X-ray tomography in the water window (Schneider *et al.*, 2010).

A limitation of the current set-up is the relatively small detection efficiency of the X-ray detection system used which is a combination of a scintillator converting X-rays to visible light and then detected with a CCD camera. New direct detection systems such as the Moench detector which is currently being developed at PSI in Switzerland will have great impact on full-field microscopy of biological samples. It will provide 100% detection efficiency also for low-energy X-rays in combination with a spatial resolution better than 2 μm. In particular, X-ray microscopy of radiation-sensitive biological samples will tremendously benefit from these developments since the dose delivered to the sample can be reduced by a factor of eight.

Portions of this research were carried out at the PETRA III light source at DESY, a member of the Helmholtz Association (HGF). The research leading to these results has received funding from the European Community's Seventh Framework Programme (FP7/2007–2013) under grant agreement No. 290605 (PSI-FELLOW/COFUND). We would also like to thank Pontus Fischer, Jan Meyer, Bernd Reime and Nicolas Stuebe for their help with the experimental set-up at beamline P11 and Dr Anja Burkhardt for assistance in using beamline P11.

References

Born, M. & Wolf, E. (1999). *Principles of Optics*, 7th ed., pp. 472–476. Cambridge University Press.

Chu, Y. S., Yi, J. M., De Carlo, F., Shen, Q., Lee, Wah-Keat, Wu, H. J., Wang, C. L., Wang, J. Y., Liu, C. J., Wang, C. H., Wu, S. R., Chien, C. C., Hwu, Y., Tkachuk, A., Yun, W., Feser, M., Liang, K. S., Yang, C. S., Je, J. H. & Margaritondo, G. (2008). *Appl. Phys. Lett.* **92**, 103119.

David, C., Kaulich, B., Barrett, R., Salomé, M. & Susini, J. (2000). *Appl. Phys. Lett.* **77**, 3851–3853.

Dierolf, M., Menzel, A., Thibault, P., Schneider, P., Kewish, C. M., Wepf, R., Bunk, O. & Pfeiffer, F. (2010). *Nature (London)*, **467**, 436–439.

Henke, B. L., Gullikson, E. M. & Davis, J. C. (1993). *At. Data Nucl. Data Tables*, **54**, 181–342.

Herker, E. & Ott, M. (2011). *Trends Endocrinol. Metab.* **22**, 241–248.

Holler, M., Raabe, J., Diaz, A., Guizar-Sicairos, M., Quitmann, C., Menzel, A. & Bunk, O. (2012). *Rev. Sci. Instrum.* **83**, 073703.

Meents, A., Reime, B., Stuebe, N., Fischer, P., Warmer, M., Goeries, D., Roever, J., Meyer, J., Fischer, J., Burkhardt, A., Vartiainen, I., Karvinen, P. & David, D. (2013). *Proc. SPIE*, **8851**, 88510K.

Neuhäusler, U., Schneider, G., Ludwig, W., Meyer, M. A., Zschech, E. & Hambach, D. (2003). *J. Phys. D*, **36**, A79–A82.

Schmahl, G., Rudolph, D., Guttmann, P., Schneider, G., Thieme, J. & Niemann, B. (1995). *Rev. Sci. Instrum.* **66**, 1282–1286.

Schneider, G., Guttmann, P., Heim, S., Rehbein, S., Mueller, F., Nagashima, K., Heymann, J. B., Müller, W. G. & McNally, J. G. (2010). *Nat. Methods*, **7**, 985–987.

Schropp, A., Hoppe, R., Patommel, J., Samberg, D., Seiboth, F., Stephan, S., Wellenreuther, G., Falkenberg, G. & Schroer, C. G. (2012). *Appl. Phys. Lett.* **100**, 253112.

Snigirev, A., Kohn, V., Snigireva, I. & Lengeler, B. (1996). *Nature (London)*, **384**, 49–51.

Stampanoni, M., Mokso, R., Marone, F., Vila-Comamala, J., Gorelick, S., Trtik, P., Jefimovs, K. & David, C. (2010). *Phys. Rev. B*, **81**, 140105.

Thibault, P., Dierolf, M., Menzel, A., Bunk, O., David, C. & Pfeiffer, F. (2008). *Science*, **321**, 379–382.

Vartiainen, I., Mokso, R., Stampanoni, M. & David, C. (2014). *Opt. Lett.* **39**, 1601–1604.

Vila-Comamala, J., Diaz, A., Guizar-Sicairos, M., Mantion, A., Kewish, C. M., Menzel, A., Bunk, O. & David, C. (2011). *Opt. Express*, **19**, 21333–21344.

Vogt, U., Lindblom, M., Charalambous, P., Kaulich, B. & Wilhein, T. (2006). *Opt. Lett.* **31**, 1465–1467.

Wang, Z., Gao, K., Chen, J., Hong, Y., Ge, X., Wang, D., Pan, Z., Zhu, P., Yun, W., Jacobsen, C. & Wu, Z. (2013). *Biotechnol. Adv.* **31**, 387–392.

Zernike, F. (1935). *Z. Tech. Phys.* **16**, 454–457.